Large Nonreciprocal Propagation of Surface Acoustic Waves in Epitaxial Ferromagnetic/Semiconductor Hybrid Structures

A. Hernández-Mínguez[1,*] F. Macià,[2] J. M. Hernàndez,[2] J. Herfort,[1] and P. V. Santos[1]

[1]*Paul-Drude-Institut für Festkörperelektronik, Leibniz-Institut im Forschungsverbund Berlin e.V., Hausvogteiplatz 5-7, 10117 Berlin, Germany*

[2]*Dept. of Condensed Matter Physics, University of Barcelona, Martí i Franquès 1, 08028 Barcelona, Spain*

Nonreciprocal propagation of sound, that is, the different transmission of acoustic waves traveling in opposite directions, is a challenging requirement for the realization of devices such as acoustic isolators and circulators. Here, we demonstrate efficient nonreciprocal transmission of surface acoustic waves (SAWs) propagating in opposite directions in a GaAs substrate coated with an epitaxial Fe_3Si film. The nonreciprocity arises from the acoustic attenuation induced by the magnetoelastic (ME) interaction between the SAW strain field and spin waves in the ferromagnetic film, which depends on the SAW propagation direction and can be controlled via the amplitude and orientation of an external magnetic field. The acoustic-transmission nonreciprocity, defined as the difference between the transmitted acoustic powers for forward and backward propagation at the ME resonance, reaches values of up to 20%, which are, to our knowledge, the largest values of nonreciprocity reported for SAWs traveling in a semiconducting piezoelectric substrate covered by a ferromagnetic film. The experimental results are well accounted for by a model for the ME interaction, which also shows that the nonreciprocity can be further enhanced by optimization of the sample design. These results make Fe_3Si/GaAs a promising platform for the realization of efficient nonreciprocal SAW devices.

I. INTRODUCTION

In recent years, there has been increasing interest in the realization of nonreciprocal acoustic systems for the efficient manipulation of sound [1]. As acoustic propagation is reciprocal in linear systems that preserve time reversibility [2], it is possible to obtain nonreciprocal transmission either by introducing nonlinear effects [3,4] or by breaking time-inversion symmetry. The latter can be achieved by, e.g., coupling the acoustic vibrations to a circulating fluid [5]. Another option for inducing local nonreciprocity is to take advantage of topologically protected acoustic modes propagating along the boundaries of periodic structures [6–9]. These approaches have been mainly demonstrated for low-frequency sound waves (less than 1 MHz) with wavelengths on the order of few millimeters, and the implementation of their working principles in miniaturized acoustic devices working at high frequencies (greater than 100 MHz) might be very challenging.

Of special interest for applications are acoustic devices based on surface acoustic waves (SAWs). SAWs are elastic vibrations propagating along the surface of a solid,

with wavelengths reaching down to the submicrometer regime and frequencies of up to several GHz. Because of their efficient piezoelectric generation and detection and their low propagation velocities, SAWs have been successfully applied in radio-frequency filters and other kinds of signal processing in on-chip acoustoelectric devices [10]. In addition to this well-established technology, SAWs are ideally suited for controlling and interfacing elementary excitations in solid-state quantum systems such as superconducting circuits [11], defect centers [12–15], and low-dimensional semiconductor structures [16–22]. Therefore, the on-demand control of the acoustic propagation direction by means of nonreciprocal devices such as SAW isolators and circulators would represent an important step towards efficient acoustic interfacing between such quantum systems.

Nonreciprocal SAW propagation has been reported in systems such as nonmagnetic metals [23] and semiconductor heterostructures [24], as well as in structures containing ferromagnetic materials [25–29]. In the first case, the nonreciprocity is caused by coupling of the lattice strain to the cyclotron motion of free carriers in a strong magnetic field, while in the second case it is related to the nonsymmetric transfer of momentum between the acoustic wave and electric currents applied parallel or antiparallel

---

*alberto.h.minguez@pdi-berlin.de

044018-1

to the SAW. In the latter case, nonreciprocal propagation is induced by coupling of the SAW strain field to the magnetization dynamics of a ferromagnet through the magnetoelastic (ME) interaction. As the magnetization precesses only clockwise around its equilibrium direction, the propagation of circularly polarized acoustic waves in the ferromagnet depends on the helicity of the strain field relative to the magnetization direction [30]. The excitation of magnetoelastic waves has been intensively studied in ferromagnetic insulators such as yttrium iron garnet (YIG) [31–35], where nonreciprocal SAW attenuation of up to two orders of magnitude was experimentally reported [25,26]. However, YIG is a weak magnetoelastic material and, in addition, the nonpiezoelectricity of YIG requires the incorporation of strongly piezoelectric films such as ZnO for the electric excitation of SAWs [25,26,36,37].

Another possibility for coupling SAWs and magnetization is the deposition of a thin ferromagnetic film on the surface of a piezoelectric substrate. This approach has been demonstrated in LiNbO$_3$ covered with a polycrystalline cobalt or nickel layer [27–29,38–44] and in ferromagnetic-semiconductor hybrid structures such as (Ga,Mn)As/GaAs [45–47]. Although nonreciprocal propagation has been demonstrated in the first case [27–29], the intrinsic structural disorder of polycrystalline Ni leads to a magnetization response with a relatively large Gilbert damping coefficient $\alpha \sim 0.05$ [48], and therefore to wide ME resonances with weak nonreciprocal effects [27,29].

Here, we present an alternative hybrid structure for ME applications consisting of an Fe$_3$Si film grown epitaxially on a GaAs substrate. Fe$_3$Si is a binary Heuslerlike ferromagnetic metal that has attracted interest as a possible component of magnetoelectronic devices [49,50]. As its cubic crystal structure is almost lattice-matched to the GaAs substrate (with a mismatch less than 0.01%), it is possible to grow epitaxial films with high interfacial perfection and structural quality [51–53], thus leading to narrow ferromagnetic resonance (FMR) lines [54, 55] characterized by damping coefficients α as low as approximately 3×10^{-4} [56]. In addition, the shear magnetoelastic coefficient b_2 for thin films of this material has been estimated to be approximately between 2 and 7 T [55]. This value is of the same order of magnitude as those of, e.g., crystalline Fe and Ni [57], thus making Fe$_3$Si a promising material for ME applications. Moreover, as SAW control and manipulation of quantum systems has mostly been demonstrated in GaAs-based semiconductor heterostructures [17–22], SAW isolators and circulators based on Fe$_3$Si/GaAs hybrids could provide an efficient integrated acoustic interface between such semiconductor-based quantum devices. Finally, in contrast to (Ga,Mn)As/GaAs, where the magnetic properties of (Ga,Mn)As require working at cryogenic temperatures [45–47,58,59], the high Curie temperature (above

800 K) [60] of Fe$_3$Si makes this material suitable for room-temperature applications.

In this paper, we demonstrate the nonreciprocal propagation of high-frequency SAWs (at 3.45 GHz) traveling in a Fe$_3$Si/GaAs hybrid structure. For well-defined orientations of the magnetization in the Fe$_3$Si film, the ME interaction transfers energy from the acoustic to the magnetic system, thus inducing SAW attenuation. The high structural quality of the film leads to very narrow ME resonance lines (i.e., with full widths at half maximum as narrow as 2 mT). The strength of the ME-induced attenuation depends on the relative angle between the magnetization orientation and the SAW wave vector. The resulting acoustic-transmission nonreciprocity, defined as the difference between the transmitted acoustic powers for forward and backward SAW propagation at the ME resonance, reaches values of up to 20%. This nonreciprocal behavior is significantly larger than that reported for Ni/LiNbO$_3$ operating at similar frequencies, thus making Fe$_3$Si/GaAs hybrids a promising platform for the realization of nonreciprocal SAW devices such as acoustic isolators and circulators in GaAs-based semiconductor heterostructures.

We organize the paper as follows. Section II describes the fabrication process and the experimental procedure. In Sec. III, we characterize the magnetic and acoustic properties of our sample, and we present experimental results on the nonreciprocal SAW propagation. In Sec. IV, we compare the results with the predictions of the theoretical model and consider the outlook. Finally, Sec. V summarizes the main results of the paper.

II. EXPERIMENTAL DETAILS

The experiments are performed on a slightly nonstoichiometric Fe$_{3+x}$Si$_{1-x}$ film with $x = 0.16$ (corresponding to a Si concentration of 21%) grown epitaxially on a GaAs(001) substrate by molecular beam epitaxy. Despite the nonstoichiometry, we refer to the material as Fe$_3$Si from now on, since the structural and magnetic properties of Fe$_{3+x}$Si$_{1-x}$ epitaxial alloys are qualitatively very similar for $-0.07 \leq x \leq 0.6$ [61,62]. We fabricate the magnetoacoustic device sketched in Fig. 1 as follows. First, a clean $c(4 \times 4)$-reconstructed GaAs surface is prepared by growing a 500-nm-thick GaAs buffer layer in a dedicated III–V semiconductor growth chamber using conventional growth parameters. The substrate is then transferred in ultrahigh vacuum to an As-free chamber, where an Fe$_3$Si film with a thickness $d = 50$ nm is grown by codeposition from high-temperature effusion cells onto the GaAs at 200°C [51]. Next, we pattern the Fe$_3$Si film by optical lithography and wet chemical etching into octagonal mesas with a distance $L = 1.2$ mm between opposite sides. In the final fabrication step, we deposit pairs of interdigital transducers (IDTs) for the generation and detection of SAWs. The IDTs are patterned on the GaAs substrate on the opposite sides
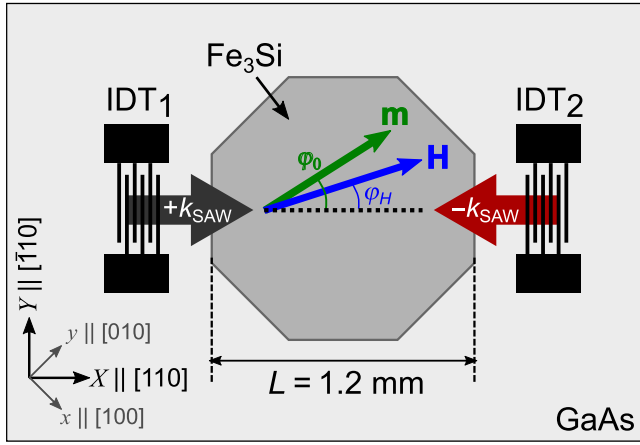
FIG. 1. Schematic illustration of the magnetoacoustic device. Interdigital transducers at opposite ends of an Fe_3Si film launch and detect SAWs with wave vectors $\pm k_{SAW}$ along the [110] crystallographic direction of the Fe_3Si/GaAs hybrid structure. The angles φ_H and φ_0 determine the orientation of the external magnetic field, **H**, and the equilibrium direction of the magnetization, **m**, with respect to the [110] surface direction.

of the octagonal Fe_3Si mesas by electron beam lithography, metal evaporation, and liftoff. Each IDT consists of 180 split-finger [10] pairs with a 150-μm-wide aperture. The finger periodicity determines the SAW wavelength, which is set to $\lambda_{SAW} = 800$ nm.

Radio-frequency (rf) signals applied to the IDTs excite SAWs propagating with a wave vector $k_{SAW} = 2\pi/\lambda_{SAW}$ parallel ($+k_{SAW}$) or antiparallel ($-k_{SAW}$) to the [110] direction of the Fe_3Si/GaAs hybrid structure. The acoustic delay line is characterized by measuring with a vector network analyzer the amplitude of the power transmission coefficient S_{21} of a SAW traveling from IDT_1 to IDT_2 ($+k_{SAW}$), as well as its counterpart S_{12} ($-k_{SAW}$). As the SAW is a Rayleigh mode, the strain tensor consists of three nonzero components ε_{XX}, ε_{ZZ}, and ε_{XZ} [63], expressed with respect to a rotated reference frame where the X, Y, and Z axes point along the [110], [$\bar{1}$10], and [001] crystallographic directions, respectively.

The ME experiments are performed by placing the magnetoacoustic device between the poles of an electromagnet for the application of a static in-plane magnetic field, **H**. The sample is mounted on an electrically controlled rotation stage that sets the angle φ_H between **H** and the [110] surface direction of the Fe_3Si/GaAs hybrid structure (see Fig. 1). The angle φ_0 determines the equilibrium direction of the magnetization $\mathbf{m} = \mathbf{M}/M_s$ (normalized to the saturation magnetization, M_s), defined as the direction that minimizes the magnetic free energy of the Fe_3Si film in the absence of SAWs (see Appendix A). For each value of φ_H and of the magnetic field strength H, we measure both the forward (S_{21}, corresponding to a wave vector $+k_{SAW}$) and the backward (S_{12}, corresponding to $-k_{SAW}$) transmission

coefficients of the SAW delay line. Then, we Fourier transform the frequency-dependent measurements into the time domain to eliminate electromagnetic crosstalk and analyze the amplitude of the SAW-related transmission peak. All measurements are performed at room temperature.

III. RESULTS

The magnetic properties of the Fe_3Si/GaAs hybrid structure are studied by FMR experiments. The color plot in Fig. 2(a) displays the dependence of the FMR signal on the static field **H** applied along [110] (horizontal axis) and on the frequency of an ac magnetic field (vertical axis) applied perpendicular to **H**. The low-magnetic-field branch
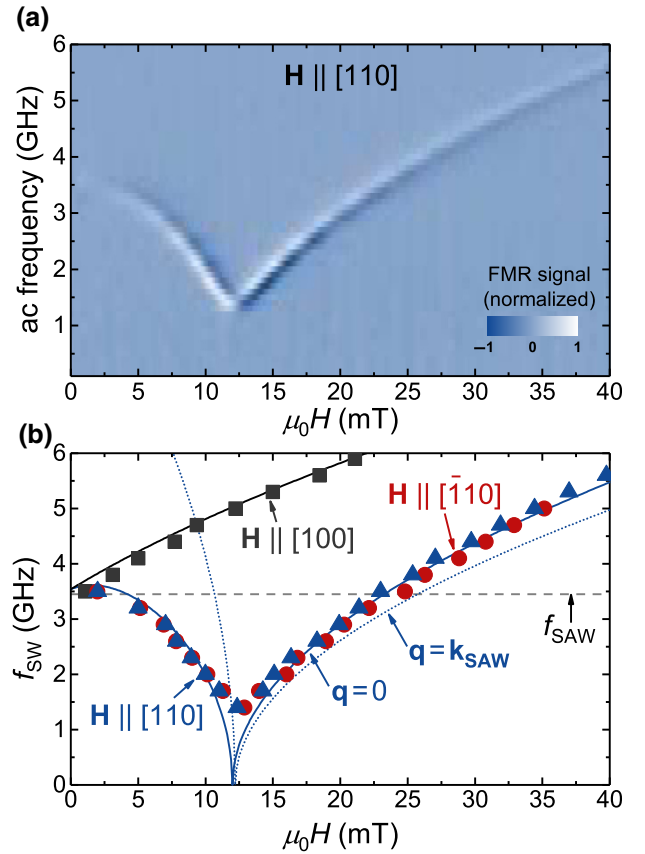

FIG. 2. (a) Dependence of the ferromagnetic resonance signal of the Fe_3Si film on the strength of a static magnetic field **H** applied along the [110] direction (horizontal axis) and the frequency of an ac field (vertical axis) applied perpendicular to **H**. (b) Spin-wave frequency, f_{SW}, as a function of the magnetic field strength when **H** is applied along [100] (black squares), [$\bar{1}$10] (red circles), and [110] (blue triangles). The solid curves are fittings supposing spin waves with wave vector $\mathbf{q} = 0$ (see Appendix A). The blue dotted curve shows the calculated frequency of spin waves with $\mathbf{q} = \mathbf{k}_{SAW}$ and **H** parallel to [110]. The horizontal dashed line indicates the SAW frequency (f_{SAW}) used in our magnetoacoustic device.

($\mu_0 H < 10$ mT) of the FMR curve represents the unsaturated state, where **m** rotates towards **H** as the magnetic field strength increases. The high-magnetic-field branch ($\mu_0 H > 10$ mT) corresponds to the saturated state, where **m** and **H** are fully aligned. This behavior indicates that the [110] direction is one of the in-plane hard axes of the magnetization. The narrow FMR lines, with a width of less than 2 mT, attest to the good structural quality and low magnetic damping of the epitaxial material [56]. Figure 2(b) summarizes the dependence of the spin-wave frequency, f_{SW}, on the magnetic field strength when **H** is applied along [100] (black squares), [$\bar{1}$10] (red circles), and [110] (blue triangles). The solid curves are fittings supposing spin waves with wave vector **q** = 0, that is, the uniform precession mode measured in the FMR experiments (see Appendix A for a description of the theoretical model). The overlap of the [110] and [$\bar{1}$10] curves confirms the negligible in-plane uniaxial anisotropy expected for the Fe concentration, growth conditions, and film thickness of this sample [54,55,64]. Therefore, the in-plane magnetization is determined only by the fourfold cubic crystalline anisotropy, with easy axes pointing along the $\langle 100 \rangle$ and hard axes along the $\langle 110 \rangle$ surface directions.

Figure 3(a) displays the dependence of S_{21} on the rf frequency applied to IDT$_1$. The measurement is time-gated to remove electromagnetic crosstalk between the IDTs. The transmission spectrum shows a minimum insertion loss of 59 dB (maximum transmission) at the resonant frequency of the IDT $f_{SAW} = v_{SAW}/\lambda_{SAW} = 3.455$ GHz, where v_{SAW} is the SAW propagation velocity in GaAs. By Fourier transforming the frequency spectrum, we obtain the profile of S_{21} in the time domain shown in Fig. 3(b) (gray dashed curve). The peak at a time delay $\Delta t \approx 610$ ns is attributed to the arrival of the SAW after traveling from IDT$_1$ to IDT$_2$. The value of Δt corresponds closely to the acoustic propagation time $\Delta l/v_{SAW}$ over the center-to-center distance ($\Delta l = 1.75$ mm) between the IDTs. The same peak is observed in the time-resolved coefficient S_{12}, i.e., for SAW transmission from IDT$_2$ to IDT$_1$ (light red dotted curve).

If the external magnetic field brings the frequency and wave vector of the spin waves in the Fe$_3$Si film into resonance with those of the SAW, then the ME interaction will excite spin waves in the ferromagnet for certain angles φ_0 between **m** and the SAW wave vector [28]. Under these conditions, the ME coupling will convert acoustic into magnetic energy as the SAW propagates in the film, thus resulting in attenuation of the SAW [27–29,40–43,46]. As indicated in Fig. 2(b), the frequency of spin waves with wave vector **q** = $\mathbf{k}_{SAW}$ (blue dotted curve) matches the SAW frequency (gray dashed line) for two different strengths of **H** applied along [110]. For **H** applied along [$\bar{1}$10], in contrast, the spin-wave frequency always lies above 10 GHz, and therefore no resonant ME coupling is possible in this magnetic configuration. In our calculations (see Appendix A), we take into account the wave-vector
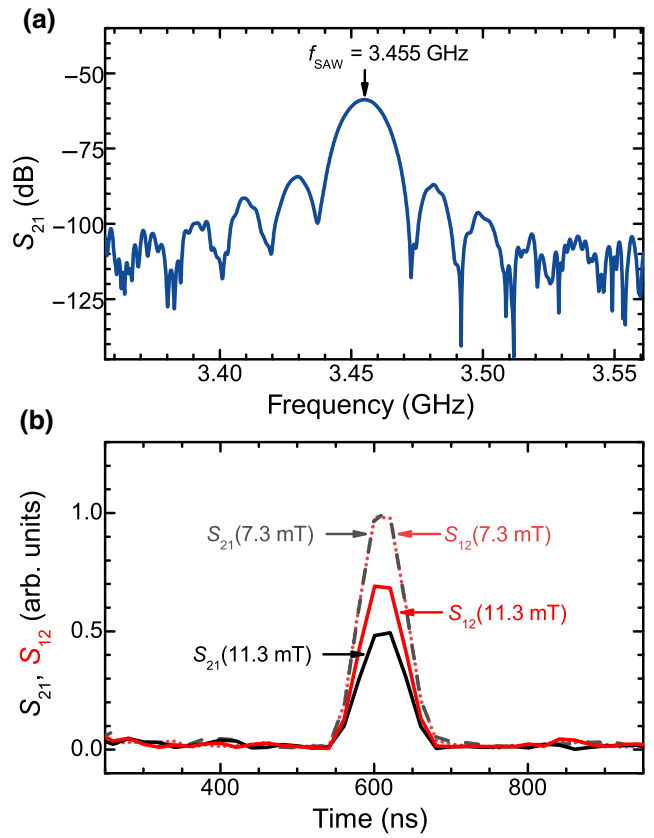

FIG. 3. (a) Dependence of scattering parameter S_{21} (corresponding to the rf power transmission coefficient) on the rf frequency applied to IDT$_1$. The spectrum is time-gated to remove electromagnetic crosstalk. The minimum insertion loss (maximum transmission) occurs at the resonance frequency $f_{SAW} = 3.455$ GHz. (b) Time-resolved coefficients S_{21} and S_{12} measured for $\varphi_H = -0.6°$ at two different magnetic field strengths. The peak delays at $\Delta t = 610$ ns correspond to the SAW propagation time between the IDTs. The curves are normalized to the magnitude of the S_{21} transmission peak for $\mu_0 H = 7.3$ mT.

dependence of the dipolar-dipolar interaction [40,65], but neglect the wave-vector dependence of the exchange interaction. This is justified because the spin-wave stiffness constant $D = 240$ meV Å^2 of Fe$_3$Si (see Ref. [66]) leads to a frequency shift $\Delta f \propto D k_{SAW}^2$ of only 36 MHz with respect to the uniform precession mode (**q** = 0) measured in the FMR experiments.

The ME coupling is investigated by measuring S_{21} and S_{12} as a function of **H** applied along the [$\bar{1}$10] and [110] directions. As expected from our calculations, we do not observe SAW attenuation for **H** parallel to [$\bar{1}$10]. In contrast, the SAW is clearly attenuated for well-defined values of **H** applied along [110]. Figure 3(b) compares the time-resolved coefficients S_{21} and S_{12} for two strengths of the magnetic field applied at an angle $\varphi_H = -0.6°$. Away from the ME resonance (for $\mu_0 H = 7.3$ mT), the intensities of the S_{21} (gray dashed curve) and S_{12} (light red dotted curve)
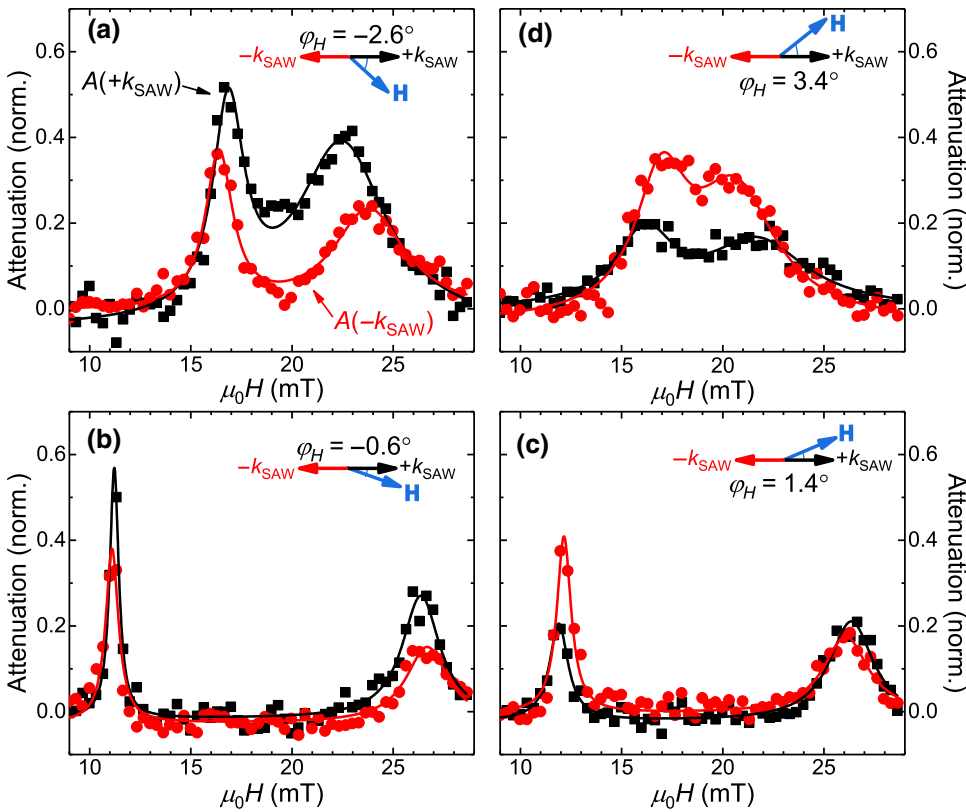
FIG. 4. Dependence of the ME-induced SAW attenuation, A, on the magnetic field amplitude, H, for SAWs with $+k_{SAW}$ (black squares) and $-k_{SAW}$ (red circles). The panels show measurements taken for magnetic field angles (a) $\varphi_H = -2.6°$, (b) $\varphi_H = -0.6°$, (c) $\varphi_H = 1.4°$, and (d) $\varphi_H = 3.4°$. The solid curves are Lorentzian fits to the ME-resonance lines.

transmission peaks are exactly the same, thus confirming the reciprocal behavior of the SAW delay line. When the magnetic field is increased to $\mu_0 H = 11.3$ mT, the acoustic and magnetic systems enter into resonance, leading to a decrease of both the S_{21} and the S_{12} peaks. Most importantly, the SAW transmission at the ME resonance is clearly different for SAWs propagating with wave vectors $+k_{SAW}$ and $-k_{SAW}$. For S_{21} (solid black curve), the ME coupling reduces the transmitted SAW power to 50% of the corresponding out-of-resonance value, while for S_{12} (solid red curve) the transmission of the SAW peak is still 70% of the out-of-resonance value. The difference between these values yields a transmission nonreciprocity of 20% for SAWs traveling in opposite directions.

To get further insight into the nonreciprocal behavior, we measure S_{21} and S_{12} for a range of H and φ_H values to determine the SAW attenuation, $A = 1 - T$. Here, T represents the area of the SAW transmission peak in the time-domain spectrum, normalized to the corresponding area for H away from the ME resonance. Figure 4 shows the dependence of $A(\pm k_{SAW})$ on H measured at four angles φ_H. Each trace shows two ME resonances at two field values. For the resonance at the low magnetic field, **m** is still rotating towards **H**, while **m** and **H** are fully aligned for the resonance at the high magnetic field. The magnetic field distance between the two resonant fields is maximum for $\varphi_H \approx 0$, and their positions agree well with the values predicted by the crossing between the spin-wave

and SAW frequencies in Fig. 2(b). As **H** rotates away from the [110] direction, the resonances move towards each other until they merge at $|\varphi_H| \approx 4°$. For larger values of φ_H, the frequency of the spin waves lies above the SAW frequency, and no ME resonances can be excited. For all four orientations of φ_H in Fig. 4, $A(+k_{SAW})$ (black squares) is clearly different from $A(-k_{SAW})$ (red circles) at the ME resonance, reaching a nonreciprocal attenuation efficiency $\Delta A = A(+k_{SAW}) - A(-k_{SAW}) \approx \pm 20\%$. Moreover, the sign of ΔA depends on the sign of the magnetic field angle: for $\varphi_H < 0$, $\Delta A > 0$ [see Figs. 4(a) and 4(b)], while for $\varphi_H > 0$ the situation reverses, and $\Delta A < 0$ [see Figs. 4(c) and 4(d)].

The two-dimensional color plots in Figs. 5(a) and 5(b) summarize the dependence of the SAW attenuation on the strength H and angular direction φ_H (see the sketch in the upper part of the figure) of the magnetic field. The resonant ME interaction (and, consequently, the SAW attenuation) takes place only in a lobe of $\varphi_H \times H$ defined by a very narrow range of angles φ_H around 0° and 180°. Figure 5(a) shows experimental data recorded for **H** directions quasiparallel (right panel, $-5° < \varphi_H < 5°$) and quasiantiparallel (left panel, $175° < \varphi_H < 185°$) to $+k_{SAW}$. Figure 5(b) displays the corresponding data for SAWs with a wave vector $-k_{SAW}$. For all configurations, the attenuation changes as the magnetic field rotates away from the [110] axis. For the quasiparallel configurations [right panel of Fig. 5(a) and left panel of Fig. 5(b)], the
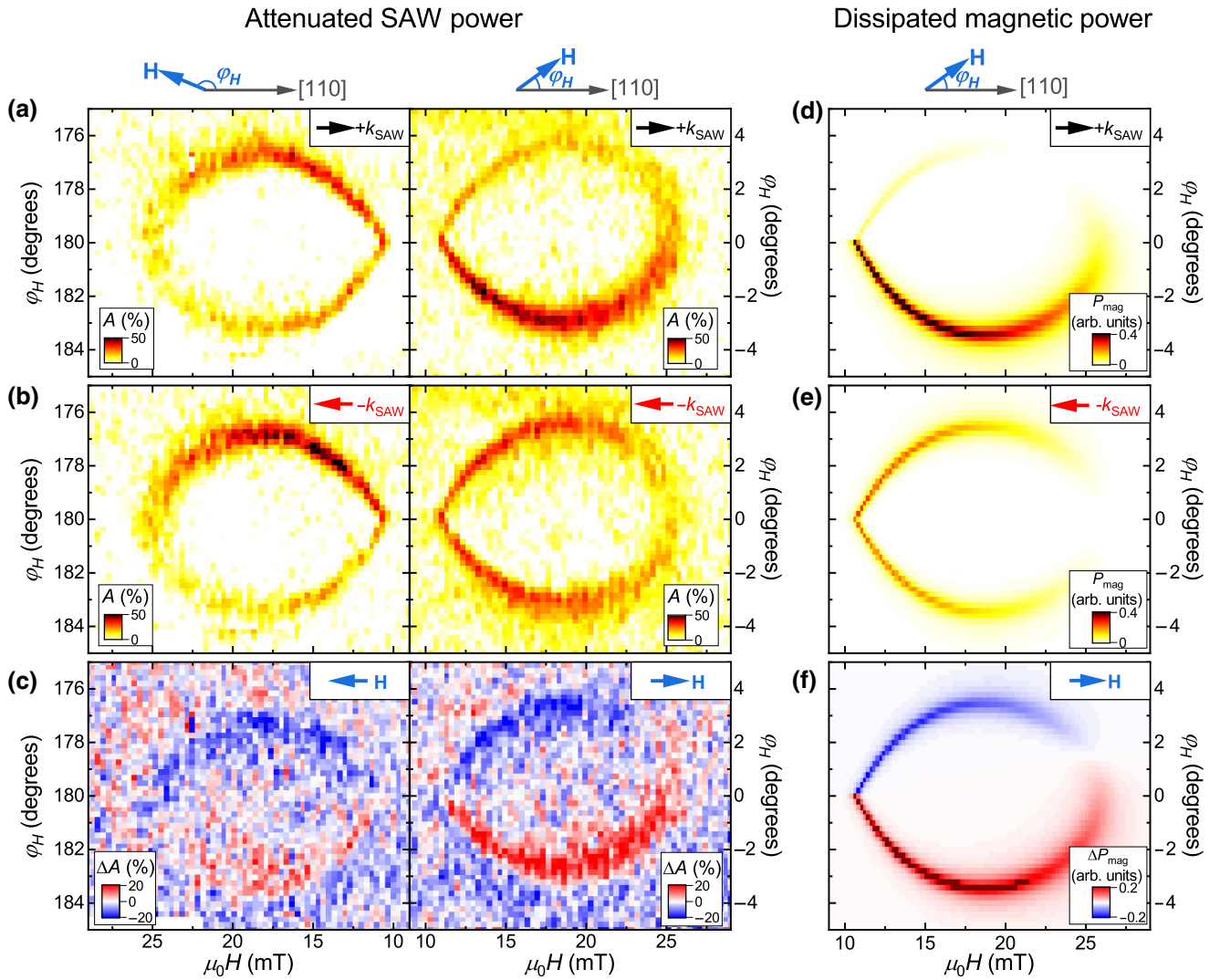
FIG. 5.   Maps of ME-induced attenuation as a function of magnetic field strength, H, and angle, φ_H, for SAWs propagating with wave vectors (a) $+k_{\mathrm{SAW}}$ and (b) $-k_{\mathrm{SAW}}$. (c) Difference in SAW attenuation, ΔA, calculated from the data in panels (a) and (b). (d) Simulation of the magnetic power dissipated in the Fe$_3$Si film, P_{mag}, as a function of H and φ_H for SAWs with a wave vector $+k_{\mathrm{SAW}}$. (e) As (d), but for SAWs with a wave vector $-k_{\mathrm{SAW}}$. (f) Difference ΔP_{mag} between panels (d) and (e).

magnitude of the attenuation is strongly angle dependent, with clearly different values in the upper and lower sides of the $\varphi_H \times H$ lobes. In the quasiantiparallel case, in contrast, the angular dependence is less pronounced. As is discussed in the next section, this weaker dependence arises from small deviations of the SAW wave vector from the [110] axis.

Finally, we show in Fig. 5(c) the nonreciprocal attenuation efficiency, ΔA, determined from the difference between the data in the corresponding panels of Figs. 5(a) and 5(b). The two panels of Fig. 5(c) show different signs of ΔA in the upper and lower sides of the $\varphi_H \times H$ lobes. As in Fig. 4, ΔA in Fig. 5(c) reaches values as large as $\pm 20\%$. Taking this value together with the length L of the ferromagnetic film, we estimate a nonreciprocal

attenuation rate $\eta \approx \Delta A / L \approx 16\%/\mathrm{mm}$. For comparison, we also estimate η from attenuation values reported for Ni/LiNbO$_3$ hybrid structures working at a SAW frequency of 2.24 GHz [27,29], obtaining $\eta \sim 1.6 \pm 0.9\%/\mathrm{mm}$. The latter is one order of magnitude lower than the values obtained in the Fe$_3$Si/GaAs structures reported here.

IV. DISCUSSION

To theoretically analyze the experimental results, we take into account the fact that, according to energy conservation, the attenuated SAW power must equal the power dissipated by the spin waves [28,42]. Therefore, as a first approximation to the problem, we just estimate the response of the magnetization to the SAW-induced ME field, and compare the power dissipated by

the spin waves with the SAW attenuation profiles in Fig. 5. The magnetization dynamics is described by the Landau-Lifshitz-Gilbert (LLG) equation [67,68],

$$\dot{\mathbf{m}} = -\gamma \mathbf{m} \times \mu_0 \mathbf{H}_{\text{eff}} + \alpha \mathbf{m} \times \dot{\mathbf{m}}, \qquad (1)$$

where μ_0 is the vacuum permeability, γ is the gyromagnetic ratio, α is the Gilbert damping constant, and the dot denotes the time derivative. The temporal evolution of $\mathbf{m}$ depends on the effective magnetic field $\mu_0 \mathbf{H}_{\text{eff}} = -\overrightarrow{\nabla}_{\mathbf{m}} F$. Here, F is the free magnetic energy normalized to the saturation magnetization. In addition to the Zeeman, shape, and crystalline anisotropy energies (see Appendix A), it includes the magnetoelastic energy, F_{me}, that couples the oscillating strain of the SAW to the magnetization. In a material with cubic symmetry, the lowest-order contributions to F_{me} can be expressed as [57]

$$F_{\text{me}} = b_1[\varepsilon_{xx} m_x^2 + \varepsilon_{yy} m_y^2 + \varepsilon_{zz} m_z^2]$$
$$+ 2b_2[\varepsilon_{xy} m_x m_y + \varepsilon_{xz} m_x m_z + \varepsilon_{yz} m_y m_z], \qquad (2)$$

where b_1 and b_2 represent the longitudinal and shear ME coefficients, respectively, while ε_{ij} and m_i are the projections of the strain and magnetization components onto the $\hat{\mathbf{x}} \parallel [100]$, $\hat{\mathbf{y}} \parallel [010]$, and $\hat{\mathbf{z}} \parallel [001]$ directions of the cubic lattice. As mentioned above, it is convenient to rewrite Eq. (2) as a function of the three nonzero strain components ε_{XX}, ε_{ZZ}, and ε_{XZ} of the SAW expressed in the rotated XYZ reference frame (see Fig. 1). We also describe $\mathbf{m}$ in spherical coordinates with azimuthal and polar angles φ and θ expressed with respect to [110] and [001], respectively. A detailed derivation of the equations is presented in Appendix B. For small angular deviations $\delta\varphi$ and $\delta\theta$ of $\mathbf{m}$ with respect to its equilibrium direction, the effective ME field driving the magnetization precession, $\mu_0 \mathbf{h} = -\overrightarrow{\nabla}_{\mathbf{m}} F_{\text{me}}$, consists of the following in-plane and out-of-plane components perpendicular to $\mathbf{m}$, i.e., h_φ and h_θ, respectively:

$$\mu_0 h_\varphi = 2b_2 \sin(\varphi_0) \cos(\varphi_0) \varepsilon_{XX}, \qquad (3)$$
$$\mu_0 h_\theta = 2b_2 \cos(\varphi_0) \varepsilon_{XZ}. \qquad (4)$$

The in-plane component h_φ is proportional to the longitudinal strain of the SAW, ε_{XX}, while the out-of-plane component h_θ is proportional to the shear strain, ε_{XZ}. Both components depend on the in-plane equilibrium direction of $\mathbf{m}$ through φ_0 (see Fig. 1). In the absence of an external magnetic field, $\mathbf{m}$ points along one of the $\langle 100 \rangle$ easy axes (i.e., $\varphi_0 = \pm 45°$). When $\mathbf{H}$ is applied along the $[\bar{1}10]$ direction, $\mathbf{m}$ rotates towards $\varphi_0 \approx 90°$, so that both h_φ and h_θ vanish. This, together with the large spin-wave frequencies expected for this magnetic configuration, explains the absence of ME coupling for this orientation of $\mathbf{H}$. In contrast, when $\mathbf{H}$ points along [110], $\mathbf{m}$ rotates

towards $\varphi_0 \approx 0$. Here, h_φ also tends to zero, but now h_θ approaches its maximum value, provided the SAW strain component ε_{XZ} is not zero. As ε_{XZ} vanishes at a free surface, h_θ is usually very small for thin ferromagnetic films and/or large SAW wavelengths, and can normally be neglected [45,69,70]. For thicker films and/or shorter SAW wavelengths, however, ε_{XZ} becomes relevant, and the contribution of h_θ to the magnetization dynamics must be taken into account. To visualize this behavior, we display in Fig. 6(a) the amplitudes of ε_{XX} and ε_{XZ} as a function of sample depth, calculated for a SAW with $\lambda_{\text{SAW}} = 800$ nm. The calculations of the SAW strain are carried out using an elastic model that takes into account the elastic properties
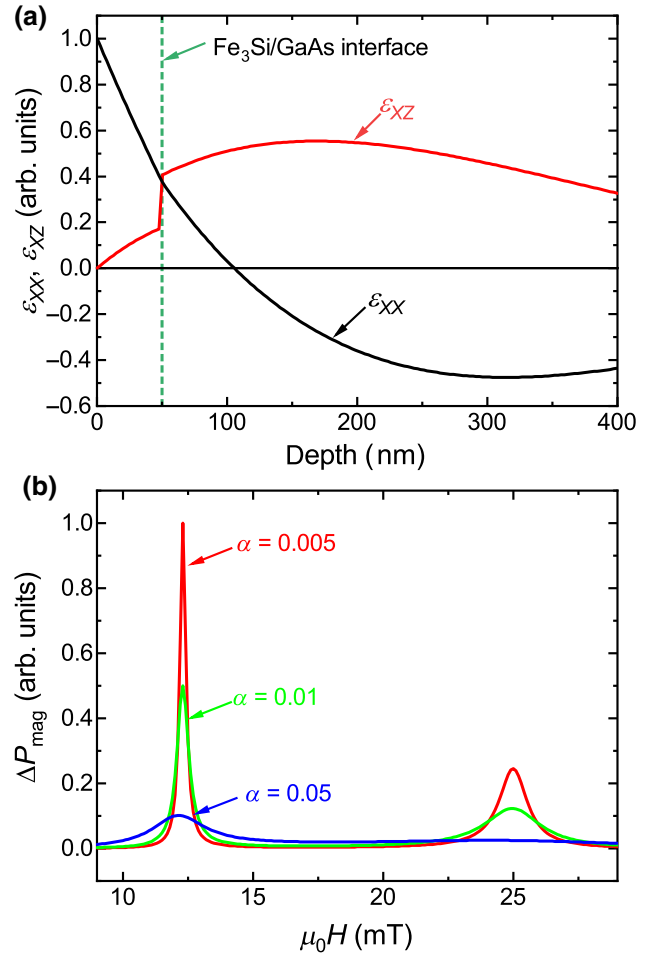

FIG. 6. (a) Dependence of the longitudinal- and shear-strain amplitudes ε_{XX} (black curve) and ε_{XZ} (red curve) on sample depth for a SAW with wavelength 800 nm. The curves are normalized with respect to the amplitude of ε_{XX} at the top surface. The vertical dashed line indicates the position of the Fe$_3$Si/GaAs interface. (b) Difference in dissipated magnetic power, ΔP_{mag}, between the parallel and antiparallel configurations of H and k_{SAW} as a function of the Gilbert damping coefficient α. The data are calculated for $f_{\text{SAW}} = 3.45$ GHz, $\varphi_H = -1.5°$, $\varepsilon_{XZ} = 0.5\varepsilon_{XX}$, and $\beta = 0$, and are normalized with respect to the maximum value for $\alpha = 0.005$.

of Fe_3Si [71] and GaAs [72]. While ε_{XX} decreases from its maximum value as one crosses the film, ε_{XZ} increases from zero and reaches a value $\varepsilon_{XZ} \approx 0.5\varepsilon_{XX}$ at the Fe_3Si/GaAs interface [marked with a vertical dashed line in Fig. 6(a)].

The observed nonreciprocal SAW attenuation can therefore be understood as an interplay between the components h_φ and h_θ [28,29]. Because of the $\pi/2$ phase shift in time between ε_{XX} and ε_{XZ} [63], the ME driving field $\mathbf{h} = h_\varphi\hat{\varphi} + ih_\theta\hat{\theta}$ is, in general, elliptically polarized. Its helicity depends on the ratio $\varepsilon_{XZ}/\varepsilon_{XX}$ and changes sign when one reverses the SAW propagation direction. As the magnetization precession described by the LLG equation has also a well-defined helicity, the strength of the ME coupling depends on the helicity of $\mathbf{h}$ [73]. For example, for a SAW propagating with $+k_{\text{SAW}}$, $\varepsilon_{XX} \propto \cos\omega t$ and $\varepsilon_{XZ} \propto \sin\omega t$. If $\mathbf{H}$ rotates the magnetization towards $0 < \varphi_0 < 45°$, then $\mathbf{h}$ and $\mathbf{m}$ precess with opposite helicities and the coupling of the SAW to the magnetization dynamics is weak; see the right panel in Fig. 5(a). However, if $\mathbf{H}$ orients $\mathbf{m}$ towards $-45° < \varphi_0 < 0$, the sign of h_φ reverses and now both $\mathbf{h}$ and $\mathbf{m}$ precess with the same helicity. Under these conditions, the ME coupling is strong, thus inducing a larger SAW attenuation. When $\mathbf{H}$ is reversed and the magnetization points against the SAW wave vector, h_θ changes sign and inverts the dependence of the helicity of $\mathbf{h}$ on φ_0. The same happens if the magnetization remains along [110] but the SAW propagates with $-k_{\text{SAW}}$, causing $\varepsilon_{XZ} \propto \sin\omega t$ to be replaced by $\varepsilon_{XZ} \propto -\sin\omega t$. Finally, when both the magnetization and the SAW wave vector are reversed, h_θ remains positive and the original dependence on the relative angle between $\mathbf{H}$ and the SAW wave vector is recovered; see the left panel in Fig. 5(b).

According to the previous discussion, the SAW attenuation profiles for quasiparallel and quasiantiparallel configurations of $\mathbf{H}$ and the SAW wave vector in Figs. 5(a) and 5(b) should be mirror images of each other. However, as already mentioned in the previous section, this is not exactly the case for the experimental data. We attribute this discrepancy to a small unintentional misalignment angle β between the SAW wave vector and the [110] direction, probably caused during the patterning of the IDTs. This misalignment breaks the symmetry of h_φ and h_θ by introducing additional terms that depend on β and b_1 (see Appendix B). As a consequence, the nonreciprocity with respect to φ_0 is enhanced in the quasiparallel configuration, but partially compensated in the quasiantiparallel configuration. To confirm this assumption, we estimate the dependence on H and φ_H of the power dissipated by the spin waves and compare it with the profiles in Figs. 5(a) and 5(b). The dissipated magnetic power, P_{mag}, can be calculated as [28]

$$P_{\text{mag}} = -\text{Im}\left[\mu_0\frac{\omega}{2}\int_{V_0}\left(\mathbf{h}^*\overline{\chi}\mathbf{h}\right)dV\right], \qquad (5)$$

where $\overline{\chi}$ is the Polder susceptibility tensor describing the response of the magnetization to $\mathbf{h}$, and V_0 is the volume of the ferromagnetic film traversed by the SAW. To obtain $\overline{\chi}$, we solve the linearized LLG equation, supposing harmonic solutions for ε_{XX}, ε_{XZ}, $\delta\theta$, and $\delta\varphi$. A detailed derivation is presented in Appendices C and D. Although an accurate calculation of P_{mag} requires an integration of $\mathbf{h}^*\overline{\chi}\mathbf{h}$ taking into account the variation of ε_{XX} and ε_{XZ} across the depth of the Fe_3Si film, we just estimate $\mathbf{h}^*\overline{\chi}\mathbf{h}$ close to the Fe_3Si/GaAs interface. This depth yields the largest ratio $\varepsilon_{XZ}/\varepsilon_{XX}$ [see Fig. 6(a)], where one expects the strongest nonreciprocal effect. In the simulation, we use values of the gyromagnetic ratio and of the shape and cubic anisotropies obtained from the fitting of the FMR curves in Fig. 2. The width of the ME resonance depends on the damping coefficient, which is set to $\alpha = 8 \times 10^{-3}$. The degree of nonreciprocity depends on the values of b_1, b_2, ε_{XX}, ε_{XZ}, and β, which we set to $b_1 = 6$ T, $b_2 = 2$ T, $\varepsilon_{XX} = 10^{-4}$, $\varepsilon_{XZ} = 0.5 \times 10^{-4}$, and $\beta = 1°$. Figures 5(d) and 5(e) display P_{mag} for $\mathbf{H}$ and the SAW wave vector in the quasiparallel and quasiantiparallel configurations, respectively, while the difference ΔP_{mag} between the two configurations is shown in Fig. 5(f). The theoretical model reflects qualitatively well the position of the ME resonances, the dependence of their amplitude on H and φ_H, and the nonreciprocal behavior.

To conclude this section, we briefly discuss the reasons for the superior nonreciprocal SAW propagation in the Fe_3Si/GaAs hybrid structure compared with polycrystalline nickel on $LiNbO_3$. The first is the high structural quality of our epitaxial Fe_3Si film, which ensures the low Gilbert damping coefficient required for the observation of these strong nonreciprocal effects. To illustrate this point, we estimate ΔP_{mag} as a function of H for a fixed value of φ_H and several values of α. The results are displayed in Fig. 6(b), normalized with respect to the maximum value for $\alpha = 0.005$. We observe that ΔP_{mag} is inversely proportional to α, and becomes 10 times smaller when α increases from 0.005 to 0.05. This is in good agreement with the difference in the calculated values of η for the Fe_3Si/GaAs and Ni/$LiNbO_3$ systems.

The second reason is the short SAW wavelength used in our experiment (800 nm), which is about 2 times smaller than that in the Ni/$LiNbO_3$(1.5 μm) structures. This implies a larger ratio $\varepsilon_{XZ}/\varepsilon_{XX}$ in the ferromagnetic film and, therefore, a larger degree of elliptical polarization of the effective ME field driving the magnetization precession. Following this approach, it should be possible to further improve the sample design to get SAW isolators with a nonreciprocal transmission exceeding 10 dB. This will happen when the SAW-induced ME field is fully circularly polarized, that is, when $|h_\varphi| = |h_\theta|$. According to Eqs. (3) and (4), this condition is fulfilled when $\varepsilon_{XZ}/\varepsilon_{XX} = \sin(\varphi_0)$. For instance, when $\varepsilon_{XZ}/\varepsilon_{XX} = 0.5$, the maximum nonreciprocity happens if an ME resonance takes place for

$\varphi_0 = 30°$. It should be possible to get close to these conditions by accurate selection of the Fe_3Si film thickness and the SAW frequency.

Finally, an alternative approach to increasing the degree of nonreciprocity has recently been proposed [74,75]. This consists in modifying the spin-wave-frequency dispersion curves, so that the frequency-crossing points for SAWs and spin waves propagating along $-k_{SAW}$ differ from those expected in the $+k_{SAW}$ case. This can be done, e.g., by covering the Fe_3Si film with a heavy-metal capping layer [74], or by fabricating structures consisting of two ferromagnetic films close to each other with opposite magnetization directions [75]. As epitaxial trilayers consisting of two Fe_3Si films separated either by a thin metal layer [76] or a semiconductor spacer [77,78] have already been reported, Fe_3Si/GaAs hybrid structures could be a promising system for the experimental implementation of this mechanism.

V. CONCLUSIONS

In this paper, we demonstrate nonreciprocal propagation of SAWs in a GaAs substrate covered with an epitaxial Fe_3Si film. For well-defined values of the external magnetic field, the magnetoelastic coupling transfers energy from the acoustic to the magnetic system, thus inducing attenuation of the SAW. The strength of the SAW attenuation depends on the relative orientation between the magnetization and the SAW wave vector, and leads to attenuation differences of up to 20% for SAWs propagating in opposite directions. We attribute the nonreciprocal behavior to the dependence of the magnetization dynamics on the helicity of the elliptically polarized magnetoelastic field associated with the SAW. Our simulations confirm these results and show that nonzero longitudinal and shear strain in the ferromagnetic film, as well as low magnetic damping, are critical to achieving large nonreciprocal effects. Because of the combination of large magnetostriction, low magnetic damping, and the possibility of growing multilayers, epitaxial Fe_3Si/GaAs hybrids are promising systems for the realization of nonreciprocal acoustic devices in GaAs-based semiconductor heterostructures.

ACKNOWLEDGMENTS

APPENDIX A: FREE MAGNETIC ENERGY

The free magnetic energy of the Fe_3Si film, normalized with respect to the saturation magnetization M_s, is expressed in spherical coordinates as [54]

$$
\begin{aligned}
F = {} & -\mu_0 H[\sin\theta \sin\theta_H \cos(\varphi - \varphi_H) + \cos\theta \cos\theta_H] \\
& - (B_d - B_{2\perp})\sin^2\theta + B_{2\|}\sin^2\theta \cos^2(\varphi - \varphi_u) \\
& - \frac{1}{2}B_{4\perp}\cos^4\theta - \frac{1}{8}B_{4\|}(3 - \cos 4\varphi)\sin^4\theta - \mu_0\mathbf{h_d}\cdot\mathbf{m}.
\end{aligned}
$$
(A1)

Here, μ_0 is the vacuum permeability, H is the strength of the external magnetic field, B_d is the shape anisotropy, $B_{4\|}$ and $B_{4\perp}$ are the fourfold in-plane and out-of-plane anisotropies, and $B_{2\|}$ and $B_{2\perp}$ are the uniaxial in-plane and out-of-plane anisotropies. The dipolar field, $\mathbf{h_d}$, accounts for the interaction caused by the time and spatial variation of the magnetization in the presence of a spin wave [40,65]. We neglect the contribution of the exchange interaction for the reasons discussed in the body of the paper. The azimuthal and polar angles φ and θ, respectively, indicate the direction of the normalized magnetization $\mathbf{m} = \mathbf{M}/M_s$, while φ_H and θ_H indicate the direction of the external magnetic field. The angle φ_u is the rotation of the easy axis of the uniaxial in-plane anisotropy with respect to the fourfold in-plane anisotropy. In our experiment, H is applied at small angles with respect to the axis defined by the [110] crystallographic direction. Therefore, we express φ, φ_H, and φ_u with respect to the [110] axis. The polar angles θ and θ_H are expressed with respect to [001]. The equilibrium direction of the normalized magnetization, $\mathbf{m}_0$, defined as the direction that minimizes Eq. (A1), is determined by φ_0 and θ_0.

The resonance frequencies ω_0 are obtained from Eq. (A1) following the Smit and Beljers formalism [79]:

$$
\omega_0^2 = \frac{\gamma^2}{1 + \alpha^2}\frac{F_{\theta\theta}F_{\varphi\varphi} - F_{\theta\varphi}F_{\varphi\theta}}{\sin^2\theta_0}.
$$
(A2)

Here, γ is the gyromagnetic ratio, α is the Gilbert damping constant, and F_{ij} stands for $\partial^2 F/\partial i\,\partial j$, calculated at $\mathbf{m}_0$. In our experiment, both the external magnetic field and the magnetization lie in the sample plane, that is, $\theta_H = \theta_0 = \pi/2$, so that $F_{\theta\varphi} = F_{\varphi\theta} = 0$. Therefore, the resonance equation for azimuthal rotation of the magnetization reads

$$
\omega_0^2 = \frac{\gamma^2}{1 + \alpha^2}F_{\theta\theta}F_{\varphi\varphi},
$$
(A3)

$$
\begin{aligned}
F_{\varphi\varphi} = {} & \mu_0 H \cos(\varphi_0 - \varphi_H) - 2B_{2\|}\cos 2(\varphi_0 - \varphi_u) \\
& - 2B_{4\|}\cos 4\varphi_0 + \mu_0 M_s \frac{qd}{2}\sin^2\varphi_0,
\end{aligned}
$$
(A4)

TABLE I. Material parameters used in the simulations of the resonant frequencies and the power dissipated by a SAW-induced spin wave.

M_s	850 kA/m
$B_{2\parallel}$	0
$B_{4\parallel}$	6.1 mT
$B_d - B_{2\perp}$	650 mT
φ_u	0
γ	1.76×10^{11} rad/T s
α	8×10^{-3}
b_1	6 T
b_2	2 T

$$F_{\theta\theta} = \mu_0 H \cos(\varphi_0 - \varphi_H) + 2(B_d - B_{2\perp})$$
$$- 2B_{2\parallel} \cos^2(\varphi_0 - \varphi_u) + \frac{1}{2}B_{4\parallel}(3 - \cos 4\varphi_0)$$
$$- \mu_0 M_s \frac{qd}{2}, \qquad (A5)$$

where q is the wave vector of the spin wave and d is the thickness of the ferromagnetic film. The ferromagnetic resonance curves in Fig. 2 are fitted assuming $q = 0$ and the material parameters displayed in Table I.

APPENDIX B: EFFECTIVE MAGNETOELASTIC FIELD

In a material with cubic symmetry, the lowest-order contributions to the magnetoelastic free energy, F_{me}, can be expressed as

$$F_{\text{me}} = b_1[\varepsilon_{xx}m_x^2 + \varepsilon_{yy}m_y^2 + \varepsilon_{zz}m_z^2]$$
$$+ 2b_2[\varepsilon_{xy}m_xm_y + \varepsilon_{xz}m_xm_z + \varepsilon_{yz}m_ym_z], \quad (B1)$$

where ε_{ij} and m_i are the projections of the strain tensor and normalized magnetization onto the $\hat{\mathbf{x}} \parallel [100]$, $\hat{\mathbf{y}} \parallel [010]$, and $\hat{\mathbf{z}} \parallel [001]$ directions of the cubic lattice.

Let us suppose that a Rayleigh wave propagates in the x-y plane in an arbitrary direction defined by the angle φ_{SAW} between $\hat{\mathbf{x}}$ and the SAW wave vector $\mathbf{k}_{\text{SAW}}$. In the rotated reference frame XYZ with $\hat{\mathbf{X}} \parallel \mathbf{k}_{\text{SAW}}$ and $\hat{\mathbf{Z}} \parallel \hat{\mathbf{z}}$, the three nonzero strain components of the SAW are ε_{XX}, ε_{ZZ}, and ε_{XZ}. We can express the components ε_{ij} in Eq. (B1) in terms of φ_{SAW}, ε_{XX}, ε_{ZZ}, and ε_{XZ} as follows:

$$\begin{array}{ll} \varepsilon_{xx} = \varepsilon_{XX}\cos^2(\varphi_{\text{SAW}}), & \varepsilon_{xy} = \varepsilon_{XX}\cos(\varphi_{\text{SAW}})\sin(\varphi_{\text{SAW}}), \\ \varepsilon_{yy} = \varepsilon_{XX}\sin^2(\varphi_{\text{SAW}}), & \varepsilon_{xz} = \varepsilon_{XZ}\cos(\varphi_{\text{SAW}}), \\ \varepsilon_{zz} = \varepsilon_{ZZ}, & \varepsilon_{yz} = \varepsilon_{XZ}\sin(\varphi_{\text{SAW}}). \end{array}$$
$$(B2)$$

In the experiment, the SAW propagates along the axis defined by the [110] direction. Therefore, we write $\varphi_{\text{SAW}} = \pi/4 + \beta$. Here, $\beta = 0$ if $\mathbf{k}_{\text{SAW}}$ is parallel to [110],

and $\beta = \pi$ if $\mathbf{k}_{\text{SAW}}$ is antiparallel to [110] (denoted in the body of the paper by $+k_{\text{SAW}}$ and $-k_{\text{SAW}}$, respectively).

As in Appendix A, we rewrite m_i in spherical coordinates with φ expressed with respect to [110] and θ with respect to [001]:

$$m_x = \sin\theta \cos(\pi/4 + \varphi),$$
$$m_y = \sin\theta \sin(\pi/4 + \varphi), \qquad (B3)$$
$$m_z = \cos\theta.$$

The effective magnetoelastic field, $\mathbf{h}$, is obtained from $\mu_0 \mathbf{h} = -\vec{\nabla}_{\mathbf{m}} F_{\text{me}}$. Here, the gradient is calculated in spherical coordinates at $\mathbf{m}_0$. The two components of $\mathbf{h}$ perpendicular to $\mathbf{m}_0$, which are therefore responsible for inducing magnetization precession, are the in-plane and out-of-plane components h_φ and h_θ, respectively. For $\theta_0 = \pi/2$ (the equilibrium magnetization lies in the sample plane), they can be written as

$$\mu_0 h_\varphi = [b_2 \cos(2\beta)\sin(2\varphi_0) - b_1 \sin(2\beta)\cos(2\varphi_0)]\varepsilon_{XX}$$
$$= f_\varphi(\varphi_0, \beta)\varepsilon_{XX}, \qquad (B4)$$

$$\mu_0 h_\theta = 2b_2 \cos(\varphi_0 - \beta)\varepsilon_{XZ} = f_\theta(\varphi_0, \beta)\varepsilon_{XZ}. \quad (B5)$$

These equations reduce to those presented in the body of the paper when $\beta = 0$.

APPENDIX C: SOLUTION OF THE LANDAU-LIFSHITZ-GILBERT EQUATION

The response of the magnetization dynamics to the driving field $\mathbf{h}$ is described by the LLG equation,

$$\dot{\mathbf{m}} = -\gamma \mathbf{m} \times \mu_0 \mathbf{H}_{\text{eff}} + \alpha \mathbf{m} \times \dot{\mathbf{m}}, \qquad (C1)$$

where the dot denotes the time derivative and the effective magnetic field is $\mu_0 \mathbf{H}_{\text{eff}} = -\vec{\nabla}_{\mathbf{m}}(F + F_{\text{me}}) = -\vec{\nabla}_{\mathbf{m}} F + \mu_0 \mathbf{h}$. Here, F is the free magnetic energy described in Eq. (A1).

Writing the LLG equation in spherical coordinates, and supposing small perturbations $\delta\theta$ and $\delta\varphi$ of the magnetization with respect to its equilibrium direction, Eq. (C1) can be linearized as

$$-\delta\dot{\theta} = \gamma\left(F_{\varphi\varphi}\,\delta\varphi - \mu_0 h_\varphi\right) + \alpha\,\delta\dot{\varphi}, \qquad (C2)$$

$$\delta\dot{\varphi} = \gamma\left(F_{\theta\theta}\,\delta\theta - \mu_0 h_\theta\right) + \alpha\,\delta\dot{\theta}, \qquad (C3)$$

where we have taken into account the fact that $\theta_0 = \pi/2$ and $F_{\varphi\theta} = F_{\theta\varphi} = 0$ in our case. Supposing that the SAW strain components can be expressed as $\varepsilon_{XX} = \varepsilon_{XX,0}e^{i\Omega}$ and $\varepsilon_{XZ} = i\varepsilon_{XZ,0}e^{i\Omega}$ with $\Omega = \mathbf{k}_{\text{SAW}} \cdot \mathbf{r} - \omega t$ and $\omega = 2\pi f_{\text{SAW}}$,

we can assume harmonic solutions of the kind $\delta\theta = \delta\theta_0 e^{i\Omega}$ and $\delta\varphi = \delta\varphi_0 e^{i\Omega}$ and rewrite Eqs. (C2) and (C3) as follows:

$$
\begin{pmatrix} \delta\theta \\ \delta\varphi \end{pmatrix} = -\mu_0 \frac{\gamma^2}{1+\alpha^2} \frac{1}{\omega^2 - \omega_0^2 + i\omega\kappa}
$$

$$
\times \begin{pmatrix} F_{\theta\theta} - i\dfrac{\omega}{\gamma}\alpha & i\dfrac{\omega}{\gamma} \\ -i\dfrac{\omega}{\gamma} & F_{\varphi\varphi} - i\dfrac{\omega}{\gamma}\alpha \end{pmatrix} \begin{pmatrix} h_\theta \\ h_\varphi \end{pmatrix}, \quad \text{(C4)}
$$

with ω_0 and κ defined as

$$
\omega_0 = \gamma \sqrt{\frac{F_{\theta\theta} F_{\varphi\varphi}}{1+\alpha^2}}, \quad \text{(C5)}
$$

$$
\kappa = \gamma \frac{\alpha}{1+\alpha^2} \left(F_{\theta\theta} + F_{\varphi\varphi} \right). \quad \text{(C6)}
$$

APPENDIX D: POWER DISSIPATED BY THE SPIN WAVES

The change in the transmitted SAW power equals the power dissipated by the spin waves, P_{mag}, which can be estimated as [28]

$$
P_{\text{mag}} = -\text{Im} \left[\mu_0 \frac{\omega}{2} \int_{V_0} (h_\theta^*, h_\varphi^*) \begin{pmatrix} \delta\theta \\ \delta\varphi \end{pmatrix} dV \right], \quad \text{(D1)}
$$

where V_0 is the volume of the ferromagnetic film traversed by the SAW. Although an accurate calculation of P_{mag} requires an integration taking into account the variation of ε_{XX} and ε_{XZ} across the depth of the Fe$_3$Si film, we just calculate the value of the integrand at the Fe$_3$Si/GaAs interface. This depth yields the largest ratio $\varepsilon_{XZ}/\varepsilon_{XX}$, and it is where one expects the strongest nonreciprocal effects.

We also neglect the decay of the strain amplitude as the SAW propagates in the ferromagnetic film at the ME resonance. Then, the power dissipated by the SAW-induced spin waves can be approximated as

$$
P_{\text{mag}} = \frac{V_0}{2} \frac{\gamma^2}{1+\alpha^2} \frac{\omega}{(\omega^2 - \omega_0^2)^2 + (\omega\kappa)^2}
$$

$$
\times \left[B\omega\kappa + C(\omega^2 - \omega_0^2) \right], \quad \text{(D2)}
$$

$$
B = F_{\varphi\varphi}(f_\theta \varepsilon_{XZ,0})^2 + F_{\theta\theta}(f_\varphi \varepsilon_{XX,0})^2 - 2\frac{\omega}{\gamma} f_\theta f_\varphi \varepsilon_{XX,0} \varepsilon_{XZ,0}, \quad \text{(D3)}
$$

$$
C = \alpha \frac{\omega}{\gamma} \left[(f_\theta \varepsilon_{XZ,0})^2 + (f_\varphi \varepsilon_{XX,0})^2 \right]. \quad \text{(D4)}
$$

The nonreciprocal behavior is related to the expression for B in Eq. (D3). If both $\varepsilon_{XX,0}$ and $\varepsilon_{XZ,0}$ are nonzero, the first and second terms of the expression for B are always positive, but the sign of the last term depends on the signs of $f_\theta(\varphi_0, \beta)$ and $f_\varphi(\varphi_0, \beta)$. To illustrate this, we show in Fig. 7 the dependence of P_{mag} on H and φ_H for several values of $\varepsilon_{XX,0}$ and $\varepsilon_{XZ,0}$, calculated using the material parameters in Table I and $\beta = 0°$.

If the SAW propagates exactly parallel or antiparallel to [110], then the profile of P_{mag} for $-k_{\text{SAW}}$ is a mirror image of the corresponding profile for $+k_{\text{SAW}}$. This is shown in Figs. 8(a) and 8(b), where we display the dependence of P_{mag} on H and φ_H for $+k_{\text{SAW}}$ ($\beta = 0°$) and $-k_{\text{SAW}}$ ($\beta = 180°$), respectively. In the calculation, we now use $\varepsilon_{XZ,0} = 0.5\varepsilon_{XX,0}$ as in the body of the paper. The mirror symmetry breaks if there is a small misalignment between $\mathbf{k}_{\text{SAW}}$ and the axis defined by the [110] direction. To illustrate this, Figs. 8(c) and 8(d) display the profiles of P_{mag} calculated
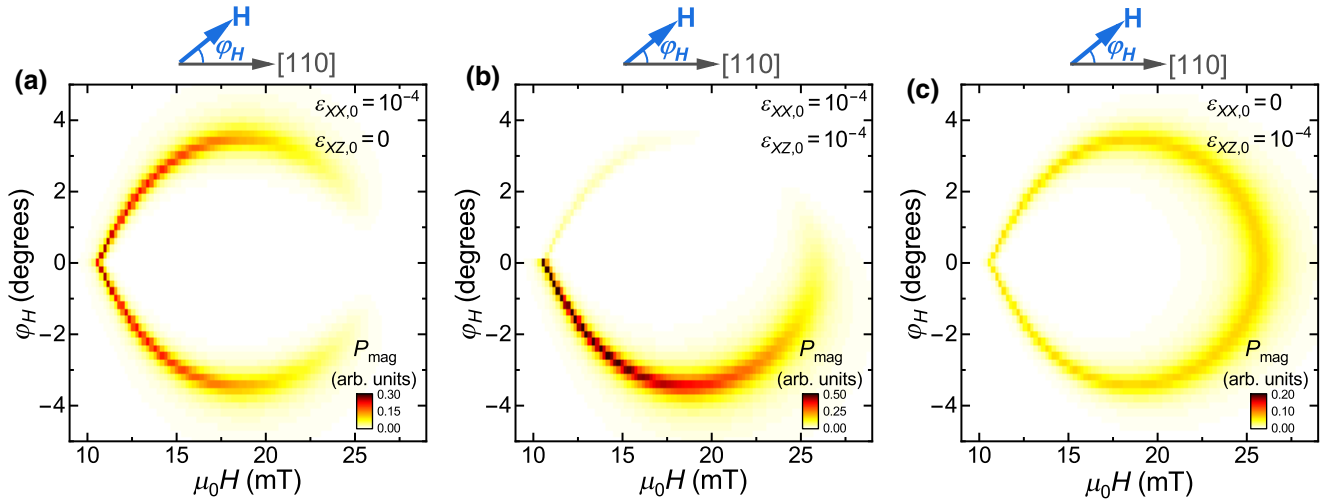

FIG. 7. Dependence of P_{mag} on H and φ_H, calculated for three different amplitudes of the longitudinal and shear strains, $\varepsilon_{XX,0}$ and $\varepsilon_{XZ,0}$, respectively. The simulations are performed with $\beta = 0°$, that is, $\mathbf{k}_{\text{SAW}}$ propagates along [110].
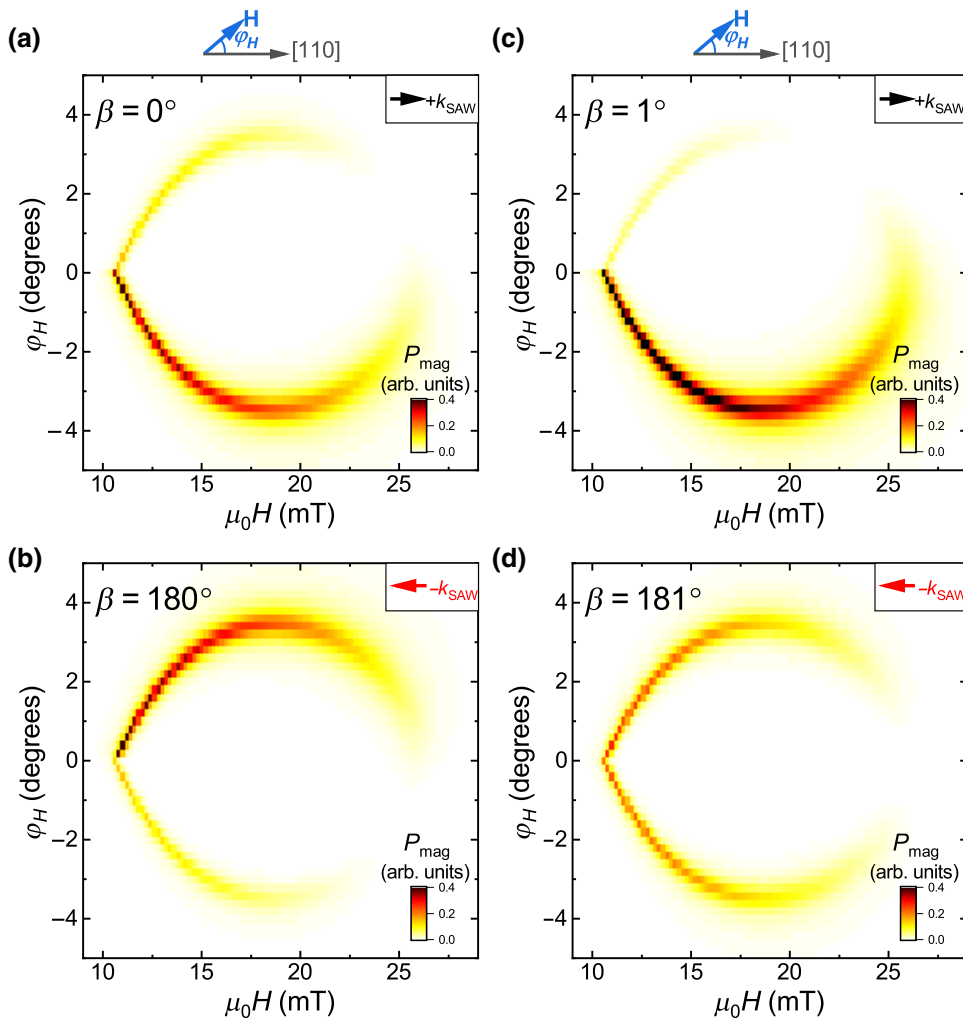
FIG. 8. Dependence of P_{mag} on H and φ_H, calculated for (a) $\mathbf{k}_{SAW}$ parallel to [110] ($\beta = 0°$, $+k_{SAW}$), (b) $\mathbf{k}_{SAW}$ antiparallel to [110] ($\beta = 180°$, $-k_{SAW}$). (c),(d) are for the same conditions as in (a),(b), but with $1°$ of misalignment added to β. The material parameters used in the calculation are the same as in Fig. 7, but now $\varepsilon_{XZ,0} = 0.5\varepsilon_{XX,0}$ as in the body of the paper.

under the same conditions as for Figs. 8(a) and 8(b), but with $1°$ of misalignment added to β.

———————————

[1] R. Fleury, D. Sounas, M. R. Haberman, and A. Alù, Nonreciprocal acoustics, Acoust. Today **11**, 14 (2015).

[2] A. Maznev, A. Every, and O. Wright, Reciprocity in reflection and transmission: What is a 'phonon diode'? Wave Motion **50**, 776 (2013).

[3] B. Liang, X. S. Guo, J. Tu, D. Zhang, and J. C. Cheng, An acoustic rectifier, Nat. Mater. **9**, 989 (2010).

[4] B.-I. Popa and S. A. Cummer, Non-reciprocal and highly nonlinear active acoustic metamaterials, Nat. Commun. **5**, 3398 (2014).

[5] R. Fleury, D. L. Sounas, C. F. Sieck, M. R. Haberman, and A. Alù, Sound isolation and giant linear nonreciprocity in a compact acoustic circulator, Science **343**, 516 (2014).

[6] A. B. Khanikaev, R. Fleury, S. H. Mousavi, and A. Alù, Topologically robust sound propagation in an angular-momentum-biased graphene-like resonator lattice, Nat. Commun. **6**, 8260 (2015).

[7] S. D. Huber, Topological mechanics, Nat. Phys. **12**, 621 (2016).

[8] H. Chen, H. Nassar, A. N. Norris, G. K. Hu, and G. L. Huang, Elastic quantum spin Hall effect in kagome lattices, Phys. Rev. B **98**, 094302 (2018).

[9] R. Fleury, M. R. Haberman, G. Huang, and A. N. Norris, Introduction to the special issue on non-reciprocal and topological wave phenomena in acoustics, J. Acoust. Soc. Am. **146**, 719 (2019).

[10] C. K. Campbell, in *Surface Acoustic Wave Devices for Mobile and Wireless Communications*, edited by R. Stern and M. Levy (Academic Press, Inc., San Diego, 1998).

[11] M. V. Gustafsson, T. Aref, A. F. Kockum, M. Ekström, G. Johansson, and P. Delsing, Propagating phonons coupled to an artificial atom, Science **346**, 207 (2014).

[12] D. A. Golter, T. Oo, M. Amezcua, K. A. Stewart, and H. Wang, Optomechanical Quantum Control of a Nitrogen-Vacancy Center in Diamond, Phys. Rev. Lett. **116**, 143602 (2016).

[13] S. J. Whiteley, G. Wolfowicz, C. P. Anderson, A. Bourassa, H. Ma, M. Ye, G. Koolstra, K. Satzinger, M. V. Holt, F. J. Heremans, A. N. Cleland, D. I. Schuster, G. Galli, and D.

D. Awschalom, Spin-phonon interactions in silicon carbide addressed by gaussian acoustics, Nat. Phys. **15**, 490 (2019).

[14] S. Lazić, A. Espinha, S. P. Yanguas, C. Gibaja, F. Zamora, P. Ares, M. Chhowalla, W. S. Paz, J. J. Palacios Burgos, A. Hernández-Mínguez, P. V. Santos, and H. P. van der Meulen, Dinamically tuned non-classical light emission from atomic defects in hexagonal boron nitride, Commun. Phys. **2**, 113 (2019).

[15] F. Iikawa, A. Hernández-Mínguez, I. Aharonovich, S. Nakhaie, Y.-T. Liou, J. M. J. Lopes, and P. V. Santos, Acoustically modulated optical emission of hexagonal boron nitride layers, Appl. Phys. Lett. **114**, 171104 (2019).

[16] C. Wiele, F. Haake, C. Rocke, and A. Wixforth, Photon trains and lasing: The periodically pumped quantum dot, Phys. Rev. A **58**, R2680 (1998).

[17] O. D. D. Couto, S. Lazić, F. Iikawa, J. A. H. Stotz, U. Jahn, R. Hey, and P. Santos, Photon anti-bunching in acoustically pumped quantum dots, Nat. Phot. **3**, 645 (2009).

[18] J. R. Gell, M. B. Ward, R. J. Young, R. M. Stevenson, P. Atkinson, D. Anderson, G. A. C. Jones, D. A. Ritchie, and A. J. Shields, Modulation of single quantum dot energy levels by a surface-acoustic-wave, Appl. Phys. Lett. **93**, 081115 (2008).

[19] E. A. Cerda-Méndez, D. N. Krizhanovskii, M. Wouters, R. Bradley, K. Biermann, K. Guda, R. Hey, P. V. Santos, D. Sarkar, and M. S. Skolnick, Polariton Condensation in Dynamic Acoustic Lattices, Phys. Rev. Lett. **105**, 116402 (2010).

[20] R. P. G. McNeil, M. Kataoka, C. J. B. Ford, C. H. W. Barnes, D. Anderson, G. A. C. Jones, I. Farrer, and D. A. Ritchie, On-demand single-electron transfer between distant quantum dots, Nature **477**, 439 (2011).

[21] S. Hermelin, S. Takada, M. Yamamoto, S. Tarucha, A. D. Wieck, L. Saminadayar, C. Bauerle, and T. Meunier, Electrons surfing on a sound wave as a platform for quantum optics with flying electrons, Nature **477**, 435 (2011).

[22] S. Lazić, A. Violante, K. Cohen, R. Hey, R. Rapaport, and P. V. Santos, Scalable interconnections for remote indirect exciton systems based on acoustic transport, Phys. Rev. B **89**, 085313 (2014).

[23] J. Heil, B. Lüthi, and P. Thalmeier, Nonreciprocal surface-acoustic-wave propagation in aluminum, Phys. Rev. B **25**, 6515 (1982).

[24] H. Zhu and M. Rais-Zadeh, Non-reciprocal acoustic transmission in a GaN delay line using the acoustoelectric effect, IEEE Electr. Dev. Lett. **38**, 802 (2017).

[25] M. F. Lewis and E. Patterson, Acoustic–surface–wave isolator, Appl. Phys. Lett. **20**, 276 (1972).

[26] M. R. Daniel, Experimental observation of nonreciprocal attenuation of surface waves in yttrium iron garnet, J. Appl. Phys. **48**, 1732 (1977).

[27] M. Weiler, L. Dreher, C. Heeg, H. Huebl, R. Gross, M. S. Brandt, and S. T. B. Goennenwein, Elastically Driven Ferromagnetic Resonance in Nickel Thin Films, Phys. Rev. Lett. **106**, 117601 (2011).

[28] L. Dreher, M. Weiler, M. Pernpeintner, H. Huebl, R. Gross, M. S. Brandt, and S. T. B. Goennenwein, Surface acoustic wave driven ferromagnetic resonance in nickel thin films: Theory and experiment, Phys. Rev. B **86**, 134415 (2012).

[29] R. Sasaki, Y. Nii, Y. Iguchi, and Y. Onose, Nonreciprocal propagation of surface acoustic wave in Ni/LiNbO₃, Phys. Rev. B **95**, 020407(R) (2017).

[30] C. Kittel, Interaction of spin waves and ultrasonic waves in ferromagnetic crystals, Phys. Rev. **110**, 836 (1958).

[31] H. Matthews and H. van de Vaart, Magnetoelastic love waves, Appl. Phys. Lett. **15**, 373 (1969).

[32] M. Tsutsumi, T. Bhattacharyya, and N. Kumagai, Piezoelectric–magnetoelastic surface wave guided by interface between semi–infinite piezoelectric and magnetoelastic media, J. Appl. Phys. **46**, 5072 (1975).

[33] P. R. Emtage, Nonreciprocal attenuation of magnetoelastic surface waves, Phys. Rev. B **13**, 3063 (1976).

[34] G. Komoriya and G. Thomas, Magnetoelastic–surface waves on YIG substrate, J. Appl. Phys. **50**, 6459 (1979).

[35] R. E. Camley, Magnetoelastic waves in a ferromagnetic film on a nonmagnetic substrate, J. Appl. Phys. **50**, 5272 (1979).

[36] Y. Shimizu, K. Hasegawas, and T. Yamada, Nonreciprocity of SAW velocity on a magnetized ferrite substrate, Electron. Commun. Jpn., Part I **63**, 1 (1980).

[37] N. I. Polzikova, S. G. Alekseev, I. I. Pyataikin, I. M. Kotelyanskii, V. A. Luzanov, and A. P. Orlov, Acoustic spin pumping in magnetoelectric bulk acoustic wave resonator, AIP Adv. **6**, 056306 (2016).

[38] A. K. Ganguly, K. L. Davis, D. C. Webb, and C. Vittoria, Magnetoelastic surface waves in a magnetic film–piezoelectric substrate configuration, J. Appl. Phys. **47**, 2696 (1976).

[39] S. Davis, A. Baruth, and S. Adenwalla, Magnetization dynamics triggered by surface acoustic waves, Appl. Phys. Lett. **97**, 232507 (2010).

[40] P. G. Gowtham, T. Moriyama, D. C. Ralph, and R. A. Buhrman, Traveling surface spin-wave resonance spectroscopy using surface acoustic waves, J. Appl. Phys. **118**, 233910 (2015).

[41] D. Labanowski, A. Jung, and S. Salahuddin, Power absorption in acoustically driven ferromagnetic resonance, Appl. Phys. Lett. **108**, 022905 (2016).

[42] P. G. Gowtham, D. Labanowski, and S. Salahuddin, Mechanical back-action of a spin-wave resonance in a magnetoelastic thin film on a surface acoustic wave, Phys. Rev. B **94**, 014436 (2016).

[43] X. Li, D. Labanowski, S. Salahuddin, and C. S. Lynch, Spin wave generation by surface acoustic waves, J. Appl. Phys. **122**, 043904 (2017).

[44] R. Sasaki, Y. Nii, and Y. Onose, Surface acoustic wave coupled to magnetic resonance on multiferroic CuB₂O₄, Phys. Rev. B **99**, 014418 (2019).

[45] L. Thevenard, J.-Y. Duquesne, E. Peronne, H. J. von Bardeleben, H. Jaffres, S. Ruttala, J.-M. George, A. Lemaître, and C. Gourdon, Irreversible magnetization switching using surface acoustic waves, Phys. Rev. B **87**, 144402 (2013).

[46] L. Thevenard, C. Gourdon, J. Y. Prieur, H. J. von Bardeleben, S. Vincent, L. Becerra, L. Largeau, and J.-Y. Duquesne, Surface-acoustic-wave-driven ferromagnetic resonance in (Ga, Mn)(As, P) epilayers, Phys. Rev. B **90**, 094401 (2014).

[47] L. Thevenard, I. S. Camara, S. Majrab, M. Bernard, P. Rovillain, A. Lemaître, C. Gourdon, and J.-Y. Duquesne, Precessional magnetization switching by a surface acoustic wave, Phys. Rev. B **93**, 134430 (2016).

[48] J. Walowski, M. D. Kaufmann, B. Lenk, C. Hamann, J. McCord, and M. Münzenberg, Intrinsic and non-local Gilbert damping in polycrystalline nickel studied by Ti:sapphire laser fs spectroscopy, J. Phys. D: Appl. Phys. **41**, 164016 (2008).

[49] J. Herfort, H.-P. Schönherr, A. Kawaharazuka, M. Ramsteiner, and K. Ploog, Epitaxial growth of $Fe_3Si/GaAs(001)$ hybrid structures for spintronic application, J. Cryst. Growth **278**, 666 (2005).

[50] A. Ionescu, C. A. F. Vaz, T. Trypiniotis, C. M. Gürtler, H. García-Miquel, J. A. C. Bland, M. E. Vickers, R. M. Dalgliesh, S. Langridge, Y. Bugoslavsky, Y. Miyoshi, L. F. Cohen, and K. R. A. Ziebeck, Structural, magnetic, electronic, and spin transport properties of epitaxial $Fe_3Si/GaAs(001)$, Phys. Rev. B **71**, 094401 (2005).

[51] J. Herfort, H.-P. Schönherr, and K. H. Ploog, Epitaxial growth of $Fe_3Si/GaAs(001)$ hybrid structures, Appl. Phys. Lett. **83**, 3912 (2003).

[52] J. Thomas, J. Schumann, H. Vinzelberg, E. Arushanov, R. Engelhard, O. G. Schmidt, and T. Gemming, Epitaxial Fe_3Si films on GaAs(100) substrates by means of electron beam evaporation, Nanotechnology **20**, 235604 (2009).

[53] C. Gusenbauer, T. Ashraf, J. Stangl, G. Hesser, T. Plach, A. Meingast, G. Kothleitner, and R. Koch, Interdiffusion in heusler film epitaxy on GaAs(001), Phys. Rev. B **83**, 035319 (2011).

[54] K. Lenz, E. Kosubek, K. Baberschke, H. Wende, J. Herfort, H.-P. Schönherr, and K. H. Ploog, Magnetic properties of $Fe_3Si/GaAs(001)$ hybrid structures, Phys. Rev. B **72**, 144411 (2005).

[55] M. Wegscheider, G. Käferböck, C. Gusenbauer, T. Ashraf, R. Koch, and W. Jantsch, Magnetic anisotropy of epitaxial $Fe_{1-x}Si_x$ films on GaAs(001), Phys. Rev. B **84**, 054461 (2011).

[56] K. Lenz, E. Kosubek, K. Baberschke, J. Herfort, H.-P. Schönherr, and K. H. Ploog, Magnetic anisotropy and resonance linewidth of $Fe_3Si/GaAs(001)$, Phys. Stat. Sol. (c) **3**, 122 (2006).

[57] R. C. O'Handley, *Modern Magnetic Materials, Principles and Applications* (John Wiler & Sons, Inc., New York, 2000), Chap. 7, p. 230.

[58] A. V. Scherbakov, A. S. Salasyuk, A. V. Akimov, X. Liu, M. Bombeck, C. Brüggemann, D. R. Yakovlev, V. F. Sapega, J. K. Furdyna, and M. Bayer, Coherent Magnetization Precession in Ferromagnetic (Ga, Mn)As Induced by Picosecond Acoustic Pulses, Phys. Rev. Lett. **105**, 117204 (2010).

[59] M. Bombeck, A. S. Salasyuk, B. A. Glavin, A. V. Scherbakov, C. Brüggemann, D. R. Yakovlev, V. F. Sapega, X. Liu, J. K. Furdyna, A. V. Akimov, and M. Bayer, Excitation of spin waves in ferromagnetic (Ga, Mn)As layers by picosecond strain pulses, Phys. Rev. B **85**, 195324 (2012).

[60] Y. Nakamura, *Landolt-Börnstein, New Series III/19c* (Springer, Berlin, 1988), p. 26.

[61] O. Kubaschewski, *Iron-Binary Phase Diagrams* (Springer, Berlin, 1982).

[62] J. Herfort, H.-P. Schönherr, K.-J. Friedland, and K. H. Ploog, Structural and magnetic properties of epitaxial $Fe_3Si/GaAs(001)$ hybrid structures, J. Vac. Sci. Technol. B **22**, 2073 (2004).

[63] L. Rayleigh, On waves propagated along the plane surface of an elastic solid, Proc. London Math. Soc. **s1-17**, 4 (1885).

[64] J. Herfort, H.-P. Schönherr, and B. Jenichen, Magnetic and structural properties of ultrathin epitaxial Fe_3Si films on GaAs(001), J. Appl. Phys. **103**, 07B506 (2008).

[65] R. L. Stamps and B. Hillebrands, Dipolar interactions and the magnetic behavior of two-dimensional ferromagnetic systems, Phys. Rev. B **44**, 12417 (1991).

[66] M. Szymanski, M. Jankowski, L. Dobrzynski, A. Wisniewski, and S. Bednarski, Spin dynamics of Fe_3Si and $Fe_{3-x}Mn_x$ alloys, J. Phys. Condens. Matter **3**, 4005 (1991).

[67] T. G. Gilbert, A lagrangian formulation of the gyromagnetic equation of the magnetic field, Phys. Rev. **100**, 1243 (1955).

[68] T. G. Gilbert, A phenomenological theory of damping in ferromagnetic materials, IEEE Trans. Magn. **40**, 3443 (2004).

[69] P. Kuszewski, I. S. Camara, N. Biarrotte, L. Becerra, J. von Bardeleben, W. S. Torres, A. Lemaître, C. Gourdon, J.-Y. Duquesne, and L. Thevenard, Resonant magneto-acoustic switching: Influence of Rayleigh wave frequency and wavevector, J. Phys. Condens. Matter **30**, 244003 (2018).

[70] P. Kuszewski, J.-Y. Duquesne, L. Becerra, A. Lemaître, S. Vincent, S. Majrab, F. Margaillan, C. Gourdon, and L. Thevenard, Optical Probing of Rayleigh Wave Driven Magnetoacoustic Resonance, Phys. Rev. Appl. **10**, 034036 (2018).

[71] G. Kötter, K. Nembach, F. Wallow, and E. Nembach, Stiffness constants and dislocation line energies and tensions of binary and ternary iron-rich Fe-Al-Si alloys, Mater. Sci. Eng., A **114**, 29 (1989).

[72] B. A. Auld, *Acoustic Fields and Waves in Solids* (Robert E. Krieger Publishing Company, Inc., Malabar, Florida, 1990).

[73] D. A. Stancil and A. Prabhakar, *Spin Waves, Theory and Applications* (Springer, Boston, 2009).

[74] R. Verba, I. Lisenkov, I. Krivorotov, V. Tiberkevich, and A. Slavin, Nonreciprocal Surface Acoustic Waves in Multilayers with Magnetoelastic and Interfacial Dzyaloshinskii-Moriya Interactions, Phys. Rev. Appl. **9**, 064014 (2018).

[75] R. Verba, V. Tiberkevich, and A. Slavin, Wide-Band Non-reciprocity of Surface Acoustic Waves Induced by Magnetoelastic Coupling with a Synthetic Antiferromagnet, Phys. Rev. Appl. **12**, 054061 (2019).

[76] B. Jenichen, U. Jahn, A. Nikulin, J. Herfort, and H. Kirmse, Structure of $Fe_3Si/Al/Fe_3Si$ thin film stacks on GaAs(001), Semicond. Sci. Technol. **30**, 114005 (2015).

[77] S. Gaucher, B. Jenichen, J. Kalt, U. Jahn, A. Trampert, and J. Herfort, Growth of $Fe_3Si/Ge/Fe_3Si$ trilayers on GaAs(001) using solid-phase epitaxy, Appl. Phys. Lett. **110**, 102103 (2017).

[78] S. Gaucher, B. Jenichen, and J. Herfort, Ferromagnet/semiconductor/ferromagnet hybrid trilayers grown using solid-phase epitaxy, Semicond. Sci. Technol. **33**, 104005 (2018).

[79] J. Smit and H. G. Beljers, Ferromagnetic resonance absorption in $BaFe_{12}O_{19}$, a highly anisotropic crystal, Philips Phys. Rep. **10**, 113 (1955).